line). Such scaling matches well with the theoretical prediction of optical Stark shift $\delta(\hbar\omega_0) = 2S{\cdot}E_p^2/\hbar\Omega$, where S is the optical Stark shift constant related to the transition dipole moment and E_p is the electric field of the pump pulse (*25*, *28*). From the experimental data, we can determine an optical Stark shift constant $S \sim 45\ D^2$ for A-exciton in monolayer WSe_2, which is of similar magnitude to that for exciton transition in semiconductor quantum wells (*29*).

The valley-selective optical Stark shift breaks the degeneracy of valley exciton transitions in monolayer WSe_2 and defines an effective valley pseudo-magnetic field. In our experiment, the photo-induced energy splitting between K and K′ exciton transitions can be as large as 10 meV (Fig. 4 and supplementary text). The corresponding pseudo-magnetic field B_{eff} for valley excitons can be estimated with $B_{eff} = \frac{\Delta E}{2g_{ex}\mu_B}$, where μ_B is the Bohr magneton and g_{ex} is the effective g-factor for valley exciton transitions in WSe_2. The effective exciton g-factor g_{ex} combines contributions from both electrons and holes and has a theoretically predicted value of ~1.5 for WSe_2 (supplementary text). Using this g-factor, we estimate a pseudo-magnetic field B_{eff} as high as 60 T for a 10-meV splitting of valley exciton transitions. A real magnetic field of this magnitude is difficult to achieve even with superconducting magnets, but such a pseudo-magnetic field for MX_2 valley excitons can be produced conveniently and with femtosecond temporal control by using light pulses.

It has been reported recently that excitons in different valleys in monolayer WSe_2, resonantly excited by linear polarization light, can maintain their phase coherence over extended time (*7*). The valley-dependent optical Stark effect offers a convenient and ultrafast way to lift the valley degeneracy and introduce a controlled phase difference between the two valley states, therefore enabling coherent rotation of resonantly excited valley polarizations with high fidelity (fig. S2). In analogy with spintronics, such coherent manipulation of valley polarization can open up fascinating opportunities for valleytronics.

REFERENCES AND NOTES

1. X. Xu, W. Yao, D. Xiao, T. F. Heinz, *Nat. Phys.* **10**, 343–350 (2014).
2. Q. H. Wang, K. Kalantar-Zadeh, A. Kis, J. N. Coleman, M. S. Strano, *Nat. Nanotechnol.* **7**, 699–712 (2012).
3. D. Xiao, G. B. Liu, W. Feng, X. Xu, W. Yao, *Phys. Rev. Lett.* **108**, 196802 (2012).
4. T. Cao *et al.*, *Nat. Commun.* **3**, 887 (2012).
5. K. F. Mak, K. He, J. Shan, T. F. Heinz, *Nat. Nanotechnol.* **7**, 494–498 (2012).
6. H. Zeng, J. Dai, W. Yao, D. Xiao, X. Cui, *Nat. Nanotechnol.* **7**, 490–493 (2012).
7. A. M. Jones *et al.*, *Nat. Nanotechnol.* **8**, 634–638 (2013).
8. Y. J. Zhang, T. Oka, R. Suzuki, J. T. Ye, Y. Iwasa, *Science* **344**, 725–728 (2014).
9. K. F. Mak, K. L. McGill, J. Park, P. L. McEuen, *Science* **344**, 1489–1492 (2014).
10. C. P. Poole, *Electron Spin Resonance* (Wiley, New York, ed. 2, 1983)
11. F. H. L. Koppens *et al.*, *Nature* **442**, 766–771 (2006).
12. J. A. Gupta, R. Knobel, N. Samarth, D. D. Awschalom, *Science* **292**, 2458–2461 (2001).
13. D. Press, T. D. Ladd, B. Zhang, Y. Yamamoto, *Nature* **456**, 218–221 (2008).
14. H. Shi *et al.*, *ACS Nano* **7**, 1072–1080 (2013).
15. Q. Wang *et al.*, *ACS Nano* **7**, 11087–11093 (2013).
16. E. J. Sie, Y.-H. Lee, A. J. Frenzel, J. Kong, N. Gedik, Biexciton formation in monolayer MoS2 observed by transient absorption spectroscopy, http://arxiv.org/abs/1312.2918 (2013).
17. C. Mai *et al.*, *Nano Lett.* **14**, 202–206 (2014).
18. J.-K. Huang *et al.*, *ACS Nano* **8**, 923–930 (2014).
19. A. Splendiani *et al.*, *Nano Lett.* **10**, 1271–1275 (2010).
20. K. F. Mak, C. Lee, J. Hone, J. Shan, T. F. Heinz, *Phys. Rev. Lett.* **105**, 136805 (2010).
21. P. Jessen, I. Deutsch, *Adv. At. Mol. Opt. Phys.* **37**, 95–138 (1996).
22. C. Cohen-Tannoudji, *Phys. Scr.* **T76**, 33 (1998).
23. D. I. Schuster *et al.*, *Phys. Rev. Lett.* **94**, 123602 (2005).
24. J. Berezovsky, M. H. Mikkelsen, N. G. Stoltz, L. A. Coldren, D. D. Awschalom, *Science* **320**, 349–352 (2008).
25. C. Cohen-Tannoudji, S. Reynaud, *J. Phys. At. Mol. Opt. Phys.* **10**, 345–363 (1977).
26. F. Wang *et al.*, *Science* **320**, 206–209 (2008).
27. K. F. Mak *et al.*, *Phys. Rev. Lett.* **101**, 196405 (2008).
28. Y.-R. Shen, *The Principles of Nonlinear Optics* (Wiley-Interscience, New York, 1984).
29. A. Von Lehmen, D. S. Chemla, J. E. Zucker, J. P. Heritage, *Opt. Lett.* **11**, 609–611 (1986).

ACKNOWLEDGMENTS

This work was supported by Office of Basic Energy Science, U.S. Department of Energy under contract DE-SC0003949 (Early Career Award) and DE-AC02-05CH11231 (Materials Science Division). L.J.L. thanks the support from Academia Sinica and National Science Council Taiwan (NSC-102-2119-M-001-005-MY3). F.W. also acknowledges the support from a David and Lucile Packard fellowship. All data described in the paper are presented in this report and supplementary materials.

SUPPLEMENTARY MATERIALS

www.sciencemag.org/content/346/6214/1205/suppl/DC1
Materials and Methods
Supplementary Text
Figs. S1 and S2
References (*30*–*34*)

30 June 2014; accepted 5 November 2014
10.1126/science.1258122

HEAVY FERMIONS

Two-dimensional Fermi surfaces in Kondo insulator SmB_6

G. Li,[1] Z. Xiang,[1,2] F. Yu,[1] T. Asaba,[1] B. Lawson,[1] P. Cai,[1,3] C. Tinsman,[1] A. Berkley,[1] S. Wolgast,[1] Y. S. Eo,[1] Dae-Jeong Kim,[4] C. Kurdak,[1] J. W. Allen,[1] K. Sun,[1] X. H. Chen,[2] Y. Y. Wang,[3] Z. Fisk,[4] Lu Li[1]*

In the Kondo insulator samarium hexaboride (SmB_6), strong correlation and band hybridization lead to an insulating gap and a diverging resistance at low temperature. The resistance divergence ends at about 3 kelvin, a behavior that may arise from surface conductance. We used torque magnetometry to resolve the Fermi surface topology in this material. The observed oscillation patterns reveal two Fermi surfaces on the (100) surface plane and one Fermi surface on the (101) surface plane. The measured Fermi surface cross sections scale as the inverse cosine function of the magnetic field tilt angles, which demonstrates the two-dimensional nature of the conducting electronic states of SmB_6.

The recent development of topological insulators is a triumph of single electron band theory (*1*–*8*). Kondo insulators can be used to explore whether similar exotic states of matter can arise in the presence of strong electronic interactions. In these strongly correlated heavy-fermion systems (*9*), the hybridization between itinerant electrons and localized orbitals opens a gap and makes the material insulating. Once the sample temperature is cold enough, the electronic structure can be mapped to a state that resembles a normal topological insulator (TI) (*10*), with a bulk insulating state and a conductive surface state. In samarium hexaboride (SmB_6), the existence of the surface state has been suggested by recent experimental observations of the surface conductance as well as a mapping of the hybridization gap (*11*–*13*). We report the observation of quantum oscillations in Kondo insulator SmB_6 using torque magnetometry via the de Haas–van Alphen (dHvA) effect. The observed Fermi surfaces are shown to be two-dimensional (2D) and arise from the crystalline (101) and (100) surfaces.

One major difference between SmB_6 and the conventional topological insulators is the crystal structure, which for SmB_6 is simple cubic (Fig. 1A). SmB_6 single crystals were grown by conventional flux methods. Each sample was etched with acid to remove the leftover flux. Figure 1B shows a photo of a piece of SmB_6 single crystal. Beside a flat (001) surface, there are four (101) planes.

We use torque magnetometry to resolve the Landau Level quantization and the resulting

[1]Department of Physics, University of Michigan, Ann Arbor, MI 48109, USA. [2]Hefei National Laboratory for Physical Science at Microscale and Department of Physics, University of Science and Technology of China, Hefei Anhui 230026, China. [3]Department of Physics, Tsinghua University, Beijing, China. [4]Department of Physics and Astronomy, University of California at Irvine, Irvine, CA 92697, USA.
***Corresponding author. E-mail: luli@umich.edu**

quantum oscillations in magnetization. Electronic transport measurements have been used to detect quantum oscillations in conventional topological materials (*14*–*22*). In contrast, magnetization is simply the derivative of the magnetic free energy G with respect to magnetic field H. Therefore, torque magnetometry probes the oscillations in the free energy and is sensitive to Fermi surface (FS) topology of both 3D and 2D electronic systems (*23*–*27*). Torque magnetometry measures directly the anisotropy of the magnetic susceptibility of a sample (*25*). With the tilted magnetic field $\vec{H}$ confined to the $\hat{a}$ - $\hat{c}$ plane, the torque τ of a paramagnet is shown as follows:

$$\tau = \mu_0\chi_a H_a H_c - \mu_0\chi_c H_c H_a = \mu_0\Delta\chi H^2 \sin\phi\cos\phi \quad (1)$$

where μ_0 is the vacuum permeability, ϕ is the tilt angle of $\vec{H}$ away from the crystalline $\hat{a}$ - $\hat{c}$ axis, and $\Delta\chi = \chi_a - \chi_c$ is the magnetic susceptibility anisotropy. Therefore, any change of the FS topology caused by the Landau Level quantization is revealed by torque magnetometry.

In our experimental setup, an SmB_6 single crystal is glued to the tip of a thin brass cantilever (Fig. 1C, inset). The magnetic torque τ is measured by tracking the capacitance change between the cantilever and a gold film underneath. An example torque τ versus magnetic field $\mu_0 H$ curve (Fig. 1C), taken at temperature T = 0.3 K and $\phi \sim 44°$, is quadratic overall, reflecting the linear H dependence of the sample magnetization and the paramagnetic nature of SmB_6. Large oscillations and small wiggles start to appear as the magnetic field goes beyond 5 T; for $\mu_0 H$ > 10 T, the fast oscillation patterns dominate.

The first question that arises is whether it is possible for the thin atomic layer of the surface state to be responsible for the observed magnitude of the magnetic torque and magnetization. The magnitude of the observed magnetic torque was recorded by the relative capacitance change, then converted to absolute values using the calibrated spring constant of the cantilevers (see supplementary materials). Figure 1D shows the field dependence of the effective magnetic moment $M \equiv \frac{\tau}{\mu_0 H}$ in a magnetic field H as high as 45 T. The maximum oscillatory M is around 3×10^{-12} A·m^2. Using the total area of all the surfaces of the SmB_6 sample, including the dominating top and bottom (100) surfaces and other small edge surfaces, we can estimate that there are 7.5×10^{11} unit cells on the sample surfaces. By normalizing the magnetic moment M to the number of surface unit cells, we find the maximum change of oscillatory M is around $\Delta M \sim 0.4\ \mu_B$ per surface unit cell, where μ_B is the Bohr magneton. The gray scale bar in Fig. 1D marks 0.5 μ_B per surface unit cell for comparison.

Our measured oscillatory M is consistent with the surface carrier density measured by the Fermi pocket size. As we will demonstrate later, the measured pocket size (300 T ~ 400 T) leads to a total carrier density of ~1×10^{14}/cm^2, which is ~0.17 electrons per unit cell. The theoretical value of the oscillatory M is 2 μ_B per electron in 2D electronic systems, confirmed experimentally in (*26*). The carrier density implies a magnetization oscillation of 0.34 μ_B per surface unit cell. Our observed maximum $\Delta M \sim$ 0.4 μ_B per surface unit cell is consistent with this simple estimate.

Figure 2 presents the oscillation pattern of the magnetic torque. The oscillatory torque τ_{OSC} is defined by subtracting a quadratic background from the torque τ. τ_{OSC} is periodic in $1/\mu_0 H$ (Fig. 2A), reflecting the quantization of the Landau Levels. The magnetic torque is measured in H up to 45 T. For metals, the oscillation frequency F is determined by the cross section area A of the Fermi surface (*23*):

$$F = \frac{\hbar}{2\pi e} A \quad (2)$$

where $\hbar$ is the reduced Planck constant, and e is the electrical charge. The fast Fourier transformation (FFT) of the oscillatory τ_{OSC}, measured at 0.3 K and $\phi \sim 32°$ (Fig. 2B) shows a number of peaks, including a small pocket α at $F^\alpha \sim 35$ T, a larger pocket β at $F^\beta \sim 300$ T, and the largest pocket γ at $F^\gamma \sim 450$ T. In the higher-frequency range, we observed a series of new features: the second harmonic of the β pocket at $2\beta \sim 600$ T and the third harmonic of the β pocket at $3\beta \sim 900$ T. Most notably, the other peak (marked as β') appears at ~520 T and arises from the oscillation due to the β pocket in a neighboring (101) surface plane. This determination is based on the angular dependence of the oscillation frequencies, as discussed in detail below and in Fig. 3.

The electronic properties of these three Fermi surfaces are revealed by tracking the temperature and field dependence of the oscillatory torque τ_{osc} (Fig. 2C). Even though an insulating gap is observed in the temperature dependence of the conductivity of SmB_6 (*11*–*13*), the temperature dependence of τ_{osc} is very much like that of a normal metal. In metals, the oscillating magnetic torque is well described by the Lifshitz-Kosevich (LK) formula (*23*). The temperature and magnetic field dependences of the oscillation amplitude are determined by the product of the thermal damping factor

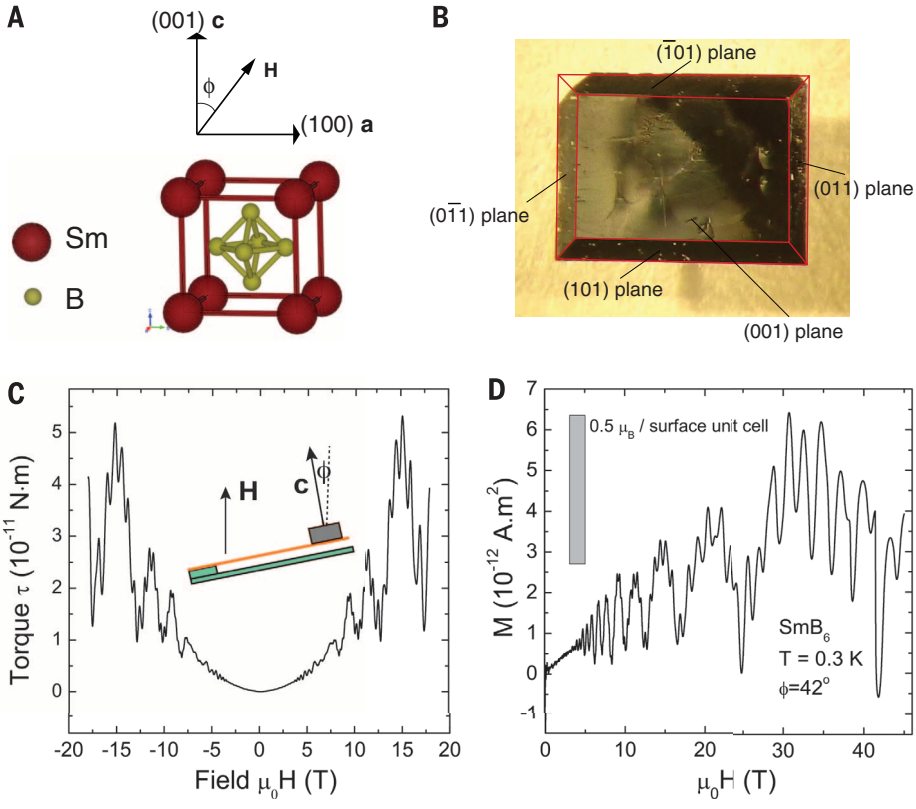

Fig. 1. Experimental setup. (**A**) The crystal structure of Kondo insulator SmB_6. The B_6 cluster and rare earth element Sm form a simple cubic structure. (**B**) Photograph of an SmB_6 single crystal. Guide lines are drawn to label the crystalline plane of each surface. (**C**) The field dependence of the magnetic torque τ in SmB_6. The data were taken at temperature T = 300 mK. Inset: sketch of the measurement setup. The sample stage is rotated to tilt magnetic field $\vec{H}$ in the crystalline $\hat{a}$ - $\hat{c}$ plane. The magnetic field was applied to the sample with a tilt angle ϕ ~44° relative to the crystalline ĉ axis. The spring constant of the cantilever was determined using the sample weight. (**D**) The field dependence of the magnetic moment M, taken at 0.3 K and under a magnetic field as high as 45 T. The low-field linear M–H dependence reflects the paramagnetism in SmB_6. The vertical gray scale bar shows the M value corresponding to 0.5 μ_B per surface unit cell.

R_T and the Dingle damping factor R_D, defined as

$$R_T = \alpha T m^*/B \sinh(\alpha T m^*/B)$$
$$R_D = \exp(-\alpha T_D m^*/B) \quad (3)$$

where the effective mass $m = m^* m_e$ and the Dingle temperature $T_D = \hbar/2\pi k_B \tau_S$. τ_S is the scattering rate, k_B is the Boltzmann Constant, m_e is the bare electron mass, $B = \mu_0 H$ is the magnetic flux density, and $\alpha = 2\pi^2 k_B m_e/e\hbar$ ~14.69 T/K (*23*).

Fitting the temperature dependence of the normalized oscillation amplitudes to the thermal damping factor R_T (Fig. 2C) yields m = $0.119m_e$ for Fermi surface α, m = $0.129m_e$ for Fermi surface β, and m = $0.192m_e$ for Fermi surface γ. Figure 2D displays the field dependence of the oscillation amplitude, normalized by the thermal damping factor R_T. Fitting the curves to R_D yields T_D ~15.9 K for Fermi surface α, T_D ~18.6 K for Fermi surface β, and T_D ~ 29.5 K for Fermi surface γ. Based on the extracted oscillation frequencies, effective masses, and Dingle temperatures, we are able to characterize the observed Fermi surfaces in SmB_6 (Table 1).

The long mean free path l measured for all three pockets (Table 1) supports the idea of intrinsic metallic surface states. The mean free path is two orders of magnitude larger than the crystal lattice constant of ~0.4 nm. Such a long mean free path is incompatible with the surface/bulk conductance arising from hopping between impurities.

The low effective mass that we measured (Table 1) is quite surprising, because most of the theoretical work on the topological Kondo insulator predicts a heavy mass of the surface states (*28*). The observed mass in SmB_6 is also much smaller than that of the divalent hexaboride compounds such as La-doped CaB_6 and EuB_6 (*29*, *30*). Pockets with heavier masses may still exist but could not be observed in our experimental conditions because of the thermal and Dingle dampings. Measurements in higher magnetic field and in colder temperatures would help resolve such extra Fermi pockets.

The most important feature of the observed quantum oscillations is the two-dimensionality (2D). For a 2D planar metallic system, the magnetic field projected to the normal axis of the plane determines the Landau Level quantizations. Thus, the oscillation frequency versus tilt angle curve generally follows the inverse of a sinusoidal function (*15*–*17*). We rotate the whole cantilever setup to track how the oscillation frequency F changes as a function of the tilt angle ϕ in a broad range of more than 180°. Using the complete FFT plots (figs. S3 to S5), we obtain the angular dependences of the oscillation frequencies of all the Fermi pockets on the (100) and (101) family surfaces, as displayed in Fig. 3, A to C.

For the dominating oscillatory pattern from pocket β, the oscillation frequency F^β not only displays a large angular dispersion but also closely tracks the 2D angular dependence from the (101) surface families. There are four branches of the $F^\beta - \phi$ patterns, as a result of the fourfold crystalline symmetry of the SmB_6 cubic structure. At each ϕ, there are two appearances of the β family. For example, at ϕ ~ 30°, there is one F^β from the (101) plane and another one from the neighboring $(\bar{1}01)$ plane (the latter contribution is marked as β′ in Fig. 2B). Most notably, all the F^β points track the solid lines of the function $F_0^\beta/\cos(\phi + 45^\circ), F_0^\beta/\cos(\phi - 45^\circ), F_0^\beta/\cos(\phi - 135^\circ)$, and $F_0^\beta/\cos(\phi - 225^\circ)$. We observe F^β at frequencies as high as 900 T—a more than 200% increase from the minimum value of 286 T. Such large divergence and the close tracking of the inverse cosine dependence strongly support the 2D nature of the observed β pocket on the (101) surface plane families.

In contrast, the angular dependence of the oscillation frequency of the α pocket F^α follows a different pattern. In Fig. 3A, the F^α values are plotted against the tilt angle ϕ of two SmB_6 single crystals. The uncertainty of F^α is determined by the half width at half-height of the F^α peak in the FFT plot. Similar to F^β, the F^α pattern has a fourfold symmetry, but the minima are located at ϕ = 0°, 90°, and 180°, that is, along the (100) crystalline axes. Fitting the data to the 2D form for this family, $F_0^\alpha/\cos(\phi - 0^\circ)$, $F_0^\alpha/\cos(\phi - 90^\circ)$, and $F_0^\alpha/\cos(\phi - 180^\circ)$, with F_0^α = 30.5 T (solid lines in Fig. 3A) results in reasonable agreement. This suggests that the observed α pocket arises from a surface state on the (100) plane families. Similarly, Fig. 3C shows that the angular dependence of the γ pocket F^γ follows the functional form of $F_0^\gamma/\cos(\phi - 0^\circ)$, $F_0^\gamma/\cos(\phi - 90^\circ)$, and $F_0^\gamma/\cos(\phi - 180^\circ)$ with F_0^γ ~385 T, suggesting the two-dimensionality of the γ pocket on the (100) surface plane.

Further, given the small value and large uncertainly of F^α, there is still a chance that an extremely elongated 3D ellipsoidal Fermi surface may fit the F^α versus ϕ dependence. Experiments with cleaner SmB_6 crystals may resolve the issue.

The angular dependence of the oscillation frequency suggests that the Fermi surface β is two-dimensional and likely arises from the crystalline (101) plane. In contrast, most of the theoretical modeling focuses on the surface states in the

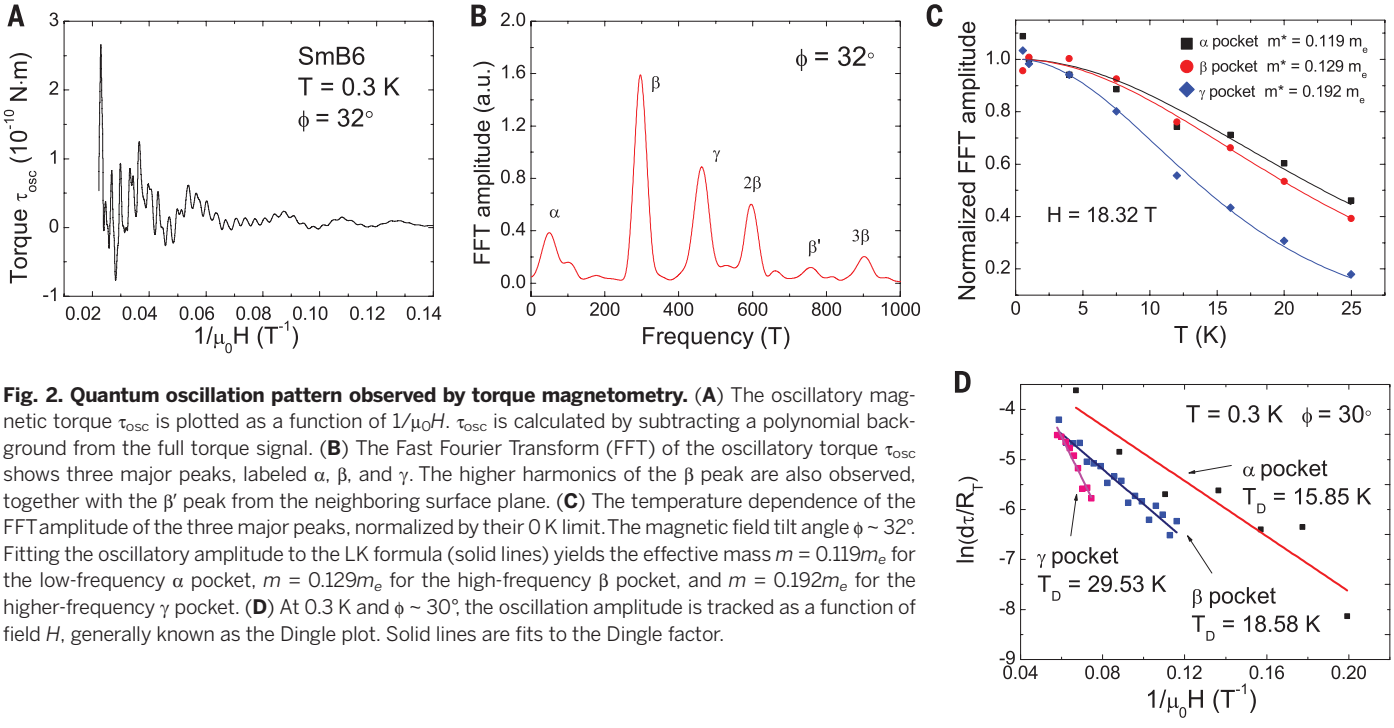

Fig. 2. Quantum oscillation pattern observed by torque magnetometry. (**A**) The oscillatory magnetic torque τ_{osc} is plotted as a function of $1/\mu_0 H$. τ_{osc} is calculated by subtracting a polynomial background from the full torque signal. (**B**) The Fast Fourier Transform (FFT) of the oscillatory torque τ_{osc} shows three major peaks, labeled α, β, and γ. The higher harmonics of the β peak are also observed, together with the β′ peak from the neighboring surface plane. (**C**) The temperature dependence of the FFT amplitude of the three major peaks, normalized by their 0 K limit. The magnetic field tilt angle ϕ ~ 32°. Fitting the oscillatory amplitude to the LK formula (solid lines) yields the effective mass $m = 0.119m_e$ for the low-frequency α pocket, $m = 0.129m_e$ for the high-frequency β pocket, and $m = 0.192m_e$ for the higher-frequency γ pocket. (**D**) At 0.3 K and ϕ ~ 30°, the oscillation amplitude is tracked as a function of field H, generally known as the Dingle plot. Solid lines are fits to the Dingle factor.

(100) planes (*31*), in which the mapping of the band inversion *X*-point gives two Fermi pocket cross sections on the (100) surface plane. Our observed α and γ pockets may be the two predicted pockets. Recent angle resolved photoemission spectroscopy (ARPES) measurements on SmB_6 revealed two Fermi pocket areas on the (100) surface Brillouin zone (*32*–*36*). Our measured Fermi surface area and the mass of pocket γ are comparable to those of a small Fermi surface centered at the Γ point and measured by ARPES. For a detailed comparison of our dHvA result and the ARPES results, see (*37*).

Questions remain as to the origin of the observed Fermi surface in the (101) plane. In the (101) plane, there are four high symmetry points [(0, 0), (0, π/a), ($\pi/\sqrt{2}a$, 0), and ($\pi/\sqrt{2}a$, π/a)]. For example (Fig. 3D), projecting the bulk band X points to the (101) plane leads to a pocket at (0, π/a) and a pair of pockets at ($\pi/\sqrt{2}a$,0) and ($-\pi/\sqrt{2}a$,0). Based on the time-reversal symmetry, only (0, π/a) has a Dirac point, which is consistent with the experimental observation. However, the topological theory does not prohibit pairs of Dirac points at low symmetry points (*37*), which offers another possible origin for the observed pockets.

The other important question is whether the 2D electronic state on the surface follows the Dirac dispersion. A general test is to track the Landau Level index plots to find out the infinite field limit, i.e., the geometric Berry phase factor. Using 45 T, the quantum limit is reached for pocket α, which, in the infinite magnetic field limit, points to −0.45 ± 0.07, very close to −1/2, the geometric Berry phase contribution, similar to other 2D Dirac electronic systems such as graphene (*18*, *19*). As the oscillation frequencies of Fermi pocket β and γ are quite close, filtering is needed to isolate the *H* dependence of the oscillation patterns for each Fermi pocket. This filtering may cause additional uncertainty of the oscillation phase, and the Zeeman effect and correlations may lead to some nonlinear effect of the Landau level index plots (*37*).

Because Al flux is used in the sample growth, the observed effective masses, oscillation frequencies, and angular dependence bear some similarity to those of pure aluminum (Al) (*38*). However, the oscillation periods of all the observed Fermi surfaces are symmetric about crystalline symmetry axes in the rotation plane. The observed fourfold symmetry and the behavior $F^{\alpha} \sim 1/\cos\phi$, $F^{\beta} \sim 1/\cos(\phi - 45^{\circ})$ and $F^{\gamma} \sim 1/\cos\phi$ cannot be explained by a residual Al impurity [for more details, see (*37*)]. Therefore, the observed quantum oscillation pattern is an intrinsic property of single-crystalline SmB_6.

We note also that our observed quantum oscillation feature is quite robust against oxidization, as the samples were always in atmosphere for storage. The ordinary surface states known to occur for vacuum clean surfaces of metal hexaborides such as LaB_6 disappear under even modest oxygen exposure (*37*, *39*).

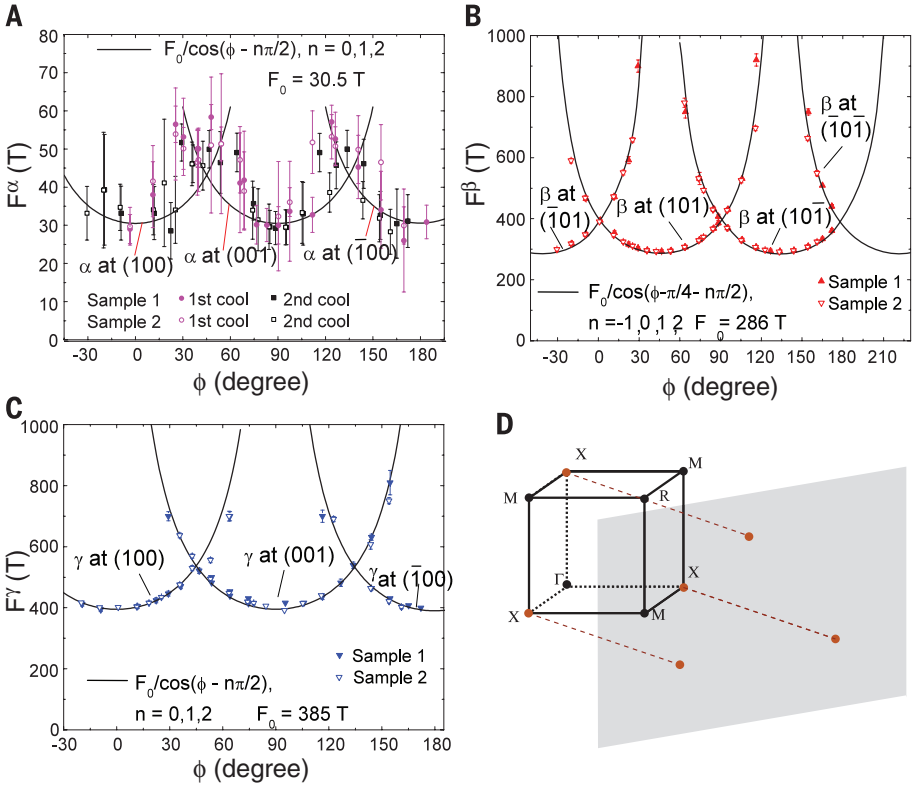

Fig. 3. Angular dependence of the oscillating frequencies in SmB_6. (**A**) Oscillation frequency F^{α} of the observed Fermi surfaces α is shown as a function of ϕ. The error bar of F^{α} is defined as the half-width at half-height of the peak in the FFT plot. To improve the statistics, two SmB_6 samples were cooled down twice. All the oscillation frequencies are inferred from the FFT spectra at many tilt angles ϕ from −30° to 180° (figs. S3 to S5) (*37*). The data are in agreement with a fit to the solid lines (described by $F_0/\cos(\phi - \phi_0)$, where ϕ_0 = 0°, 90°, and 180°). The lines correspond to 2D Fermi surfaces on the surface planes (100), (001), and (−1 0 0). (**B**) Oscillation frequency F^{β} of the observed Fermi surfaces β measured in two SmB_6 samples. F^{β} is consistent with the expected 2D Fermi surface sitting at the four surface planes of the (101) surface family. The solid line is the fitting curve $F_0/\cos(\phi - \phi_0)$, where ϕ_0 = −45°, 45°, 135°, and 225°. (**C**) The angular dependence of the oscillation frequency F^{γ} of the pocket γ. Solid lines are fits to $F_0/\cos(\phi - \phi_0)$ with ϕ_0 = 0°, 90°, and 180°. (**D**) Sketch of the Brillouin zone of SmB_6. Band inversion occurs at the *X* points. The projection of these *X* points to the (101) plane shows a possible location of the Fermi surfaces in the (101) surface state.

Table 1. Parameters in the three Fermi pockets in SmB_6. The oscillation frequency *F* and Fermi wavevector k_F are obtained from the dHvA period. The effective mass *m*, Fermi velocity v_F, mean free path *l*, and the mobility μ are inferred from the *T* and *H* dependences of the oscillation amplitude. The Landau level index plot yields the infinite field limit δ.

	α	β	γ
F (T)	29.3 ± 4	286 ± 5	385 ± 5
Crystalline surface Origin	(1 0 0)	(1 0 1)	(1 0 0)
k_F (nm^{-1})	0.30 ± 0.02	0.941 ± 0.008	1.080 ± 0.011
m/m_e	0.119 ± 0.007	0.129 ± 0.004	0.192 ± 0.005
v_F ($10^5 ms^{-1}$)	2.90 ± 0.39	8.45 ± 0.33	6.50 ± 0.21
l (nm)	22 ± 8	52 ± 6	25 ± 4
μ ($\times 10^3$ $cm^2/V{\cdot}s$)	1.1 ± 0.5	0.84 ± 0.10	0.36 ± 0.05
$k_F l$	6.6 ± 2.9	49 ± 6	27 ± 4
δ	−0.45 ± 0.07	−0.44 ±0.06	−0.32 ± 0.07

REFERENCES AND NOTES

1. L. Fu, C. L. Kane, E. J. Mele, *Phys. Rev. Lett.* **98**, 106803 (2007).
2. X.-L. Qi, T. L. Hughes, S.-C. Zhang, *Phys. Rev. B* **78**, 195424 (2008).
3. J. E. Moore, L. Balents, *Phys. Rev. B* **75**, 121306 (2007).
4. D. Hsieh *et al.*, *Nature* **452**, 970–974 (2008).
5. Y. L. Chen *et al.*, *Science* **325**, 178–181 (2009).
6. M. König *et al.*, *Science* **318**, 766–770 (2007).
7. M. Z. Hasan, C. L. Kane, *Rev. Mod. Phys.* **82**, 3045–3067 (2010).
8. X.-L. Qi, S. C. Zhang, *Rev. Mod. Phys.* **83**, 1057–1110 (2011).

9. A. Menth, E. Buehler, T. H. Geballe, . *Phys. Rev. Lett.* **22**, 295–297 (1969).
10. M. Dzero, K. Sun, V. Galitski, P. Coleman, *Phys. Rev. Lett.* **104**, 106408 (2010).
11. S. Wolgast *et al.*, *Phys. Rev. B* **88**, 180405 (2013).
12. D. J. Kim *et al.*, *Sci. Rep.* **3**, 3150 (2013).
13. X. Zhang *et al.*, *Phys. Rev. X* **3**, 011011 (2013).
14. J. G. Checkelsky *et al.*, *Phys. Rev. Lett.* **103**, 246601 (2009).
15. K. Eto, Z. Ren, A. A. Taskin, K. Segawa, Y. Ando, *Phys. Rev. B* **81**, 195309 (2010).
16. J. Analytis *et al.*, *Nat. Phys.* **6**, 960–964 (2010).
17. D. X. Qu, Y. S. Hor, J. Xiong, R. J. Cava, N. P. Ong, *Science* **329**, 821–824 (2010).
18. K. S. Novoselov *et al.*, *Nature* **438**, 197–200 (2005).
19. Y. Zhang, Y. W. Tan, H. L. Stormer, P. Kim, *Nature* **438**, 201–204 (2005).
20. B. Sacépé *et al.*, *Nat. Commun.* **2**, 575 (2011).
21. J. Xiong *et al.*, *Phys. Rev. B* **86**, 045314 (2012).
22. K. Behnia, L. Balicas, Y. Kopelevich, *Science* **317**, 1729–1731 (2007).
23. D. Shoenberg, Magnetic Oscillations in Metals. (Cambridge Univ. Press, Cambridge, UK, 1984).
24. S. E. Sebastian *et al.*, *Nature* **454**, 200–203 (2008).
25. L. Li *et al.*, *Science* **321**, 547–550 (2008).
26. J. P. Eisenstein *et al.*, *Phys. Rev. Lett.* **55**, 875–878 (1985).
27. S. A. J. Wiegers *et al.*, *Phys. Rev. Lett.* **79**, 3238–3241 (1997).
28. V. Alexandrov, M. Dzero, P. Coleman, *Phys. Rev. Lett.* **111**, 226403 (2013).
29. M. C. Aronson, J. Sarrao, Z. Fisk, M. Whitton, B. Brandt, *Phys. Rev. B* **59**, 4720–4724 (1999).
30. D. Hall *et al.*, *Phys. Rev. B* **64**, 233105 (2001).
31. F. Lu, J. Zhao, H. Weng, Z. Fang, X. Dai, *Phys. Rev. Lett.* **110**, 096401 (2013).
32. N. Xu *et al.*, *Phys. Rev. B* **88**, 121102 (2013).
33. M. Neupane *et al.*, *Nat. Commun.* **4**, 2991 (2013).
34. J. Jiang *et al.*, *Nat. Commun.* **4**, 3010 (2013).
35. E. Frantzeskakis *et al.*, *Phys. Rev. X* **3**, 041024 (2013).
36. J. D. Denlinger *et al.*, Temperature dependence of linked gap and surface state evolution in the mixed valent topological insulator SmB6. http://arxiv.org/abs/1312.6637 (2013).
37. Additional information may be found in the supplementary materials on *Science* Online.
38. C. O. Larson, W. L. Gordon, *Phys. Rev.* **156**, 703–715 (1967).
39. See, for example, B. Nishitani, *et al., Surface Science* **95**, 341 (1980).

ACKNOWLEDGMENTS

This study is based on work supported by the U. S. Department of Energy (DOE) under Award no. DE-SC0008110 (high-field torque magnetometry), by the startup fund and the Mcubed project at the University of Michigan (low-field magnetization characterization), and by the NSF DMR-0801253 and Univ. of California–Irvine CORCL grant MIIG-2011- 12-8 (Z. F. group, sample growth). Part of the work performed at the University of Michigan was supported by NSF grant DMR-1006500 (C.K. group, device fabrication) and by NSF grant ECCS-1307744 (L.L. group, device transport characterization). Z.X. and X.H.C. thank the China Scholarship Council for support and the National Basic Research Program of China (973 Program, grant no. 2012CB922002). B.L. thanks the NSF graduate research fellowship (F031543) for support. T.A. thanks the Nakajima Foundation Scholarship for support. The Corbino samples were fabricated at the Lurie Nanofabrication Facility (LNF), a member of the National Nanotechnology Infrastructure Network, which is supported by the NSF. The high-field experiments were performed at the National High Magnetic Field Laboratory, which is supported by NSF Cooperative Agreement no. DMR-084173, by the State of Florida, and by the DOE.

SUPPLEMENTARY MATERIALS

www.sciencemag.org/content/346/6214/1208/suppl/DC1
Materials and Methods
Supplementary Text
Figures S1 to S14
Table S1
Equation S1
References (*40*–*50*)

2 January 2014; accepted 5 November 2014
10.1126/science.1250366

CHEMICAL KINETICS

Predictive a priori pressure-dependent kinetics

Ahren W. Jasper,[1] Kenley M. Pelzer,[2] James A. Miller,[2] Eugene Kamarchik,[1] Lawrence B. Harding,[2] Stephen J. Klippenstein[2]*

The ability to predict the pressure dependence of chemical reaction rates would be a great boon to kinetic modeling of processes such as combustion and atmospheric chemistry. This pressure dependence is intimately related to the rate of collision-induced transitions in energy *E* and angular momentum *J*. We present a scheme for predicting this pressure dependence based on coupling trajectory-based determinations of moments of the *E*,*J*-resolved collisional transfer rates with the two-dimensional master equation. This completely a priori procedure provides a means for proceeding beyond the empiricism of prior work. The requisite microcanonical dissociation rates are obtained from ab initio transition state theory. Predictions for the $CH_4 = CH_3 + H$ and $C_2H_3 = C_2H_2 + H$ reaction systems are in excellent agreement with experiment.

Pressure-dependent reactions are ubiquitous in applications of gas-phase chemical kinetics to practical problems, such as combustion (<100 bar), atmospheric chemistry (≤1 bar), and chemical vapor deposition (<<1 bar). These reactions can take various forms involving chemical or thermal activation, single or multiple unimolecular potential wells, and single or multiple sets of bimolecular products. Such reactions are enormously complicated problems to treat theoretically, even for a single-channel, single-well dissociation, which is the case we focus on here. The accurate first-principles prediction of pressure-dependent rate coefficients would dramatically improve the utility of theoretical kinetics as a tool for global chemical modeling.

There are two constants of motion in an isolated dissociating molecule: the total internal (vibrational-rotational) energy, *E*, and the total angular momentum, *J*. A physically correct description of the kinetics requires a quantitative understanding of the rate of collision-induced transitions in these two variables, $k_c(E,J;E',J')$, and the corresponding *E*- and *J*-resolved dissociation/isomerization rate constant, $k(E,J)$. The master equation treats the time dependence of the state-resolved species populations arising from collisions and dissociation. This time dependence can be directly related to pressure-dependent thermal dissociation rate constants $k(T,p)$ (*1*–*4*).

Although many of the foundational formulations of reaction rate theory considered pressure dependence, subsequent theoretical developments have almost exclusively focused on pressure-independent reactions. Such pressure-independent rate coefficients are generally obtained from a thermal average of $k(E,J)$ and are independent of the collisional transition process. Many classes of pressure-independent reactions can now be treated with very high accuracy. For example, quantitative first-principles kinetics calculations for pressure-independent bimolecular reactions of three- and four-atom (*5*–*7*) and larger systems (*8*) have been highlighted as milestones in the development of reaction rate theory. For larger systems, ab initio transition state theory provides high-accuracy predictions for the high-pressure addition rates as illustrated, for example, in our recent studies of $O(^3P)$ + alkenes (*9*), of $^1CH_2$ + alkenes (*10*), and of alkyl radical + alkyl radical reactions (*11*), where a priori theory and experiment agreed to within 20%. In contrast, accurate first-principles methods for predicting pressure-dependent reaction rates have not been similarly developed.

In the low-pressure limit, $k(T,p)$ is independent of $k(E,J)$ and is instead determined by the details of the collision-induced transitions in *E* and *J* (*12*). At intermediate pressures, both the collision-induced transition rates and the decomposition rates play an important role in the kinetics. Prior theoretical kinetics work has employed simple empirical models for the collisional transition rates, with parameters adjusted to reproduce available experimental data (*13*, *14*). This empiricism severely limits the utility of theoretical kinetics as a mechanism development tool. Empirical theories are effectively limited to interpolations and extrapolations of the pressure and temperature ranges for reactions that have already been studied experimentally. Correlation of the energy transfer parameters with physical properties (e.g., molecular size, collision bath gas, reaction temperature) provides some predictive ability, but currently such correlations are not well determined and introduce additional uncertainties in the rate estimates of at least a factor of 2. For example, information regarding the temperature dependence of the energy transfer parameters is very limited, especially for temperatures that deviate strongly from 300 K. Furthermore, for complex multiple-well, multiple-product reactions, the effects of the uncertainties in such correlations are greatly

[1]Combustion Research Facility, Sandia National Laboratories, MS 9055, Livermore, CA 94551-0969, USA. [2]Chemical Sciences and Engineering Division, Argonne National Laboratory, Argonne, IL 60439, USA.
***Corresponding author. E-mail: sjk@anl.gov**

Two-dimensional Fermi surfaces in Kondo insulator SmB_6

G. Li *et al.*

Science **346**, 1208 (2014);
DOI: 10.1126/science.1250366